# A Constant Current Control Method With Improved Dynamic Performance for *CLLC* Converters

Huan Chen, *Student Member, IEEE*, Kai Sun, *Senior Member, IEEE*, Languang Lu, Shuoqi Wang, and Minggao Ouyang

***Abstract*—The capacitor–inductor–inductor–capacitor (*CLLC*) converter is a promising topology for bidirectional power conversion applications, such as hydrogen or battery energy storage systems and bidirectional pulsing current charging or heating for electric vehicle (EV) batteries. For these applications, high dynamic constant current control is required. In this article, a novel constant current control method with improved dynamic performance over the conventional proportional–integral (PI) method is proposed for the *CLLC* converter. In constant current control, the charging and discharging process of the output capacitor determines the dynamic performance. A state trajectory model is proposed for the *CLLC* converter and is employed to analyze the transient process in the resonant tank. Based on the analysis, a novel dead-band-based control method for the constant current control is proposed. The proposed method can directly and effectively control the charging and the discharging process of the output capacitor, which the conventional PI control method cannot do. As a result, the dynamic performance is improved. The correctness of the proposed state trajectory model, the state trajectory analysis, and the effectiveness of the proposed constant current control method are verified by experiments. Experimental results show that the response time of the proposed method is reduced by more than 50% compared with that of the conventional PI method, with no overshoot.**

***Index Terms*—*CLLC* converter, constant current control, dynamic performance, state trajectory analysis.**

## I. Introduction

THE capacitor-inductor-inductor-capacitor (*CLLC*) converter is a high-frequency, high-power density, isolated bidirectional dc–dc converter. The *CLLC* converter is regarded as a promising topology for bidirectional power transmission because of its excellent soft-switching characteristics [1], [2]. The application fields of the *CLLC* converter include uninterrupted power supply systems, dc distribution systems, vehicle-to-grid systems, electric aircrafts, and reversible solid oxide fuel cell systems [1]–[8].

The detailed operating process and basic characteristics of *CLLC* are introduced in [1], [2]. Currently, research on the *CLLC* converter is mainly focused on two aspects. One is hardware improvement. For this aspect, researchers have mainly concentrated on parameter design [2], [3], [9], [10], transformer design [11]–[14], and topology improvement [15], [16]. Parameter design is one of the hottest issues in hardware improvement. Typically, a symmetric resonant tank is designed to obtain uniform bidirectional characteristics [2], [10]. Asymmetric resonant tanks are usually used for special purposed. In order to improve power density, an equivalent method is proposed to simplified the symmetric resonant tank to an asymmetric resonant tank that does not have the secondary side resonant inductor [3]. In [9], an asymmetric parameters methodology is proposed for *CLLC* converters to narrow the switching frequency range for wide output range applications. The second is the control method. Traditionally, pulse frequency modulation (PFM) + proportional–integral (PI) control is used to regulate the voltage or the current [1], [2]. Based on that, researchers have proposed several control methods to improve control performance. A pulse width modulation (PWM) control strategy was proposed to achieve a higher voltage gain [17]. Phase shift control was analyzed and applied for *CLLC* converters [18]. Hybrid strategies combining phase-shifting control and frequency modulation were proposed to reduce reactive power and improve dynamic performance [19], [20]. A comprehensive sliding mode control loop design for the *CLLC* converter was proposed to improve converter dynamics and achieve tight output voltage regulation [21]. A hybrid compensation scheme was proposed to reduce the influence of gate drive delay and improve power conversation efficiency [22]. Several synchronous rectification methods were proposed to reduce the power loss of the secondary side rectifier bridge [23], [24].

However, these newly proposed control methods are aimed at voltage regulation. In applications like hydrogen or battery energy storage systems [25] and bidirectional pulsing current charging or heating for electric vehicle (EV) batteries [26], bidirectional power transmission is needed, and good dynamic performance is also required in these applications when load or current target changes suddenly. For *CLLC* converters, the constant current control is realized by a PI controller at present. However, it is difficult to obtain a fast and consistent transient response using a conventional PI controller because resonant

Manuscript received January 21, 2021; revised May 3, 2021 and July 15, 2021; accepted August 13, 2021. Date of publication August 30, 2021; date of current version October 15, 2021. This work was supported in part by the National Natural Science Foundation of China under Grant 51877117 and in part by Tsinghua-Toyota Joint Research Institute Cross-Discipline Program. Recommended for publication by Associate Editor D. Maksimovic. *(Corresponding author: Kai Sun.)*

Huan Chen and Kai Sun are with the State Key Lab of Power Systems, Department of Electrical Engineering, Tsinghua University, Beijing 100084, China (e-mail: chenh18@mails.tsinghua.edu.cn; sun-kai@mail.tsinghua.edu.cn).

Languang Lu, Shuoqi Wang, and Minggao Ouyang are with the School of Vehicles and Mobility, Tsinghua University, Beijing 100084, China. (e-mail: lulg@mail.tsinghua.edu.cn; wang-sq2013@qq.com; ouymg@mail.tsinghua.edu.cn).

Color versions of one or more figures in this article are available at https://doi.org/10.1109/TPEL.2021.3108631.

Digital Object Identifier 10.1109/TPEL.2021.3108631

converters usually have inconsistent dynamic behavior at different gains or different switching frequencies [27]. Thus, a new constant current control method with improved dynamic performance is needed.

Reported works on constant current control are mainly for other topologies. *LLC* converters with constant current control were proposed for LEDs and ozone-driven systems, but the conventional PI method was used and the dynamic performance was not investigated [28], [29]. A high dynamic parabolic current control method was proposed for voltage source inverters [30], and a high dynamic current control method based on the synchronization of zero-crossing current ripples was proposed for multiphase buck converters [31]. However, *CLLC* topology is quite different from the researched topologies in [30] and [31], and the ideas proposed in [30] and [31] are hard to implement in the *CLLC* converter.

In order to achieve good dynamic performance, an accurate analysis of the transient process in the resonant tank is essential. Researchers have proposed several analysis methods for the *CLLC* converter. The first harmonic approximation method [2], [23] and the extended harmonic approximation method [24] are both frequency domain methods. They are convenient for analyzing the gain characteristics but are imprecise for the modeling of the operating process. The operation mode method [9], [32] is a time domain method, which is accurate in analyzing the steady state waveforms in the resonant tank. However, the operation mode method relays on numerical iteration, and using the operation mode method to analyze the transient process in the resonant tank is complicated.

The state trajectory method is effective for describing and analyzing the transient process in the resonant tank. The state trajectory method was first employed in the series resonant converter [33], and then it was developed for the *LLC* converter [34]. With the state trajectory method, the transient process of the *LLC* resonant tank can be expressed graphically, which greatly simplifies the analysis. A series of high dynamic performance control methods was proposed for the *LLC* converter based on the state trajectory method [35]–[37]. Although the *CLLC* converter can be seen as the bidirectional version of the *LLC* converter [38], the resonant tank of the *CLLC* converter is more complicated than that of *LLC* converters, and the state trajectory models for *LLC* converters are not suitable for the *CLLC* converter.

In this article, the state trajectory method is developed for the *CLLC* converter. By introducing new state variables in the state trajectory analysis, the equivalent circuit of the *CLLC* converter is simplified and a state trajectory model for the *CLLC* converter is established. A comprehensive state trajectory analysis of the load transient process under constant current control is proposed. Based on the analysis of the transient process, a novel dead-band-based control method is proposed for constant current control. The proposed constant current control method can achieve direct control of the charging or discharging current of the output capacitor during the load transient. As a result, the dynamic performance of the proposed constant current control method is an obvious improvement over the conventional PI control method. The control diagram comparison of the conventional PI control method and the proposed dead-band-based control method is illustrated in Fig. 1. The correctness of the proposed state trajectory model, the state trajectory analysis, and the effectiveness of the proposed constant current control method were verified by experiments.

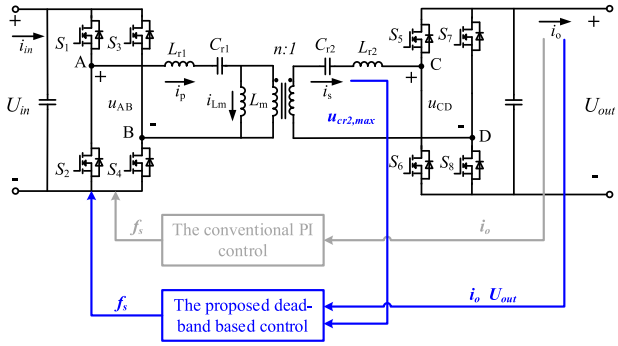


Fig. 1. Control diagram comparison of the conventional PI control method and the proposed dead-band-based control method.

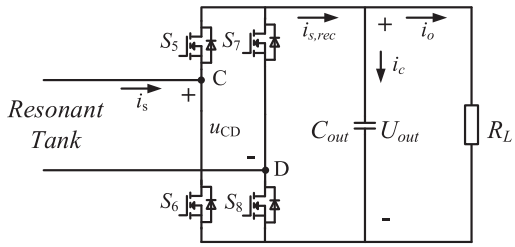


Fig. 2. Diagram of the output side.

The rest of this article is organized as follows. In Section II, the load transient process at the output side under constant current control is analyzed first. Then, the state trajectory model for the *CLLC* converter is proposed, and a state trajectory analysis of the dynamic process in the resonant tank during the load transient is given. In Section III, the proposed dead-band-based constant current control method is analyzed. In Section IV, experimental results are provided to verify the proposed dead-band-based constant current method. Finally, Section V concludes this article.

## II. Load Transient Analysis for Constant Current Control in *CLLC* Converters

### A. Load Transient Process Under the Constant Current Control

Fig. 1 shows the topology of the *CLLC* converter. $S_1$ to $S_4$ are the primary side switches and $S_5$ to $S_8$ are the secondary side switches. The primary side and secondary side current are indicated by $i_p$ and $i_s$, respectively. $U_{in}$ and $i_{in}$ are input voltage and input current, respectively. Positive directions of the voltage and current used in the analysis are also given, and the transformer turns ratio is $n$. The proposed method addresses the case where the switching frequency is not larger than the resonant frequency ($f_s \leq f_r$, i.e., the voltage gain $\geq 1$).

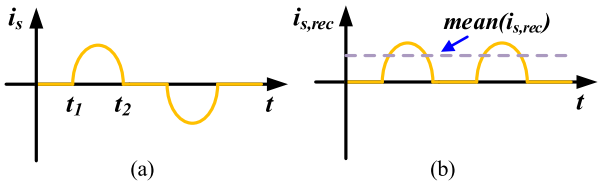


Fig. 3. (a) Waveform of $i_s$. (b) Waveform of $i_{s,rec}$.

TABLE I
LOAD TRANSIENT PROCESSES UNDER CONSTANT CURRENT CONTROL

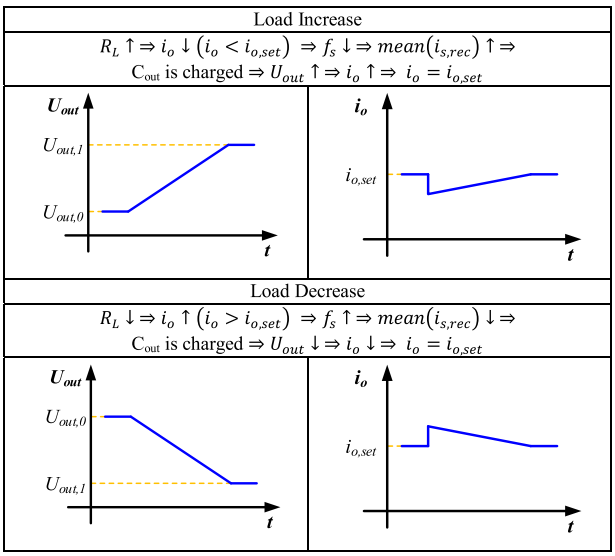


Fig. 2 shows the diagram of the output side. $U_{\rm out}$ and $i_o$ are the output voltage and output current, respectively. $C_{\rm out}$ is the output capacitor. The charging and discharging current of $C_{\rm out}$ is indicated by $i_c$. Fig. 3 shows the waveforms of $i_s$ and $i_{s,rec}$. The rectified current of $i_s$ is indicated by $i_{s,rec}$, and the mean value of $i_{s,rec}$ is indicated by $\mathrm{mean}(i_{s,rec})$. The value of $\mathrm{mean}(i_{s,rec})$ can be calculated using (1). In the steady state, $\mathrm{mean}(i_{s,rec})$ equals $i_o$, and $U_{\rm out}$ stays constant

$$\mathrm{mean}\ (i_{s,rec}) = \frac{2}{T_s}\int_{t_1}^{t_2} i_s dt. \tag{1}$$

In constant current control, the controller of the converter tries to maintain $i_o$ at the target value $i_{o,\rm set}$. Since $i_o$ is constant, the larger the load resistance $R_L$ is, the larger the output power will be. The load increase and load decrease transient processes under constant current control are listed in Table I.

In the case of a load increase, $R_L$ increases suddenly. $U_{\rm out}$ is the voltage across $C_{\rm out}$, so $U_{\rm out}$ will not change at the load increase moment (i.e., $U_{\rm out} = U_{\rm out,0}$ ). As a result, $i_o$ will drop (i.e., $i_o < i_{o,\rm set}$). The drop of $i_o$ will be detected by the controller instantly. For *CLLC* converters, the lower the switching frequency is, the larger the voltage gain will be [1], [2]. Therefore, the controller will set $f_s$ to lower values, and $\mathrm{mean}(i_{s,rec})$ will increase and be larger than $i_o$. Consequently, $C_{\rm out}$ will be charged, $U_{\rm out}$ will increase, and $i_o$ will increase. Finally, $i_o$ will equal to $i_{o,\rm set}$, and $U_{\rm out}$ will equal $U_{\rm out,1}$.

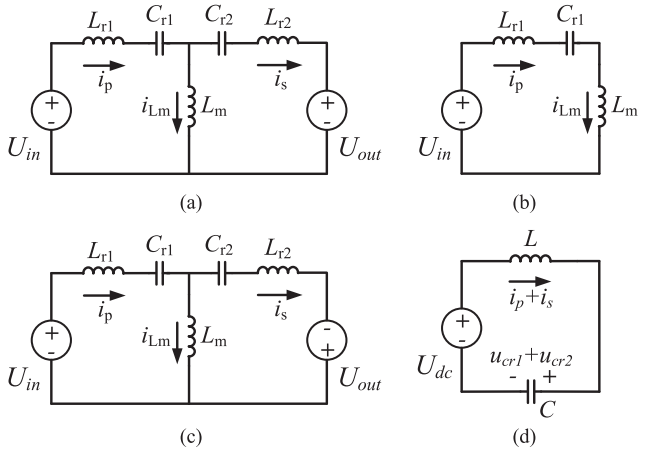


Fig. 4. (a) Equivalent circuit of the P Mode. (b) Equivalent circuit of the O Mode. (c) Equivalent circuit of the N Mode. (d) Unified equivalent circuit for the P, N, and O Modes.

Similarly, in the situation of a load decrease, $R_L$ decreases suddenly, and $i_o$ increases. The controller will set $f_s$ to higher values, so $C_{\rm out}$ will be discharged, and $i_o$ will decrease until it equals $i_{o,\rm set}$.

According to the analysis above-mentioned, the charging and discharging process of $C_{\rm out}$ determines the dynamic performance during the load transient. Two factors influence the charging and discharging process of $C_{\rm out}$. One is the capacitance of $C_{\rm out}$; the other is the charging and discharging current $i_c$. The capacitance of $C_{\rm out}$ is a constant value, which is a design parameter not related to the control method. As a result, only $i_c$ needs to be taken into consideration. According to Fig. 2, $i_c$ can be calculated as follows:

$$i_c = \mathrm{mean}\,(i_{s,rec}) - i_o. \tag{2}$$

When $i_c > 0$, $C_{\rm out}$ is charged. When $i_c < 0$, $C_{\rm out}$ is discharged.

### *B. State-Trajectory Model for CLLC Converters*

The state trajectory model for the *LLC* converter is based on the different operation modes. Similar with the *LLC* converter, the operating process of *CLLC* converters can also be divided into the P, N, and O Modes [32]. However, the resonant tank of the *CLLC* converter is more complicated than that of the *LLC* converter. For the O Mode, the operating process is an *LC* resonance, which is similar with the *LLC* converter. But for the P Mode and N Mode, the operating processes are a more complicated four-order resonance instead of a simple *LC* resonance. As a result, the state-trajectory model for the *LLC* converter cannot be applied to the *CLLC* converter directly. To solve this problem, the state-trajectory method is developed and a state-trajectory model is proposed for the *CLLC* converter.

Equivalent circuits of the P, O, and N Modes for the *CLLC* converter are illustrated in Fig. 4(a)–(c). The transformer turns ratio $n$ is set at 1 for simplicity.

By defining the base value for the voltage, the current, and the impedance as

$$z_{\text{base}} = \sqrt{L_{r1}/C_{r1}} = \sqrt{L_{r2}/C_{r2}}\,, \quad u_{\text{base}} = U_{in}\,, \quad i_{\text{base}} = \frac{u_{\text{base}}}{z_{\text{base}}}\,. \tag{3}$$

The per-unit form time domain expressions of $i_p$, $i_s$, $u_{cr1}$, $u_{cr2}$ in P Mode can be expressed as

$$\begin{cases} i_p\ (\phi) = P_1\cos\phi - P_2\sin\phi + k_1P_4\sin(k_1\phi) \\ \qquad\qquad +P_3\cos(k_1\phi) \\ i_s\ (\phi) = P_1\cos\phi - P_2\sin\phi - k_1P_4\sin(k_1\phi) \\ \qquad\qquad -P_3\cos(k_1\phi) \\ u_{cr1}\ (\phi) = P_1\sin\phi + P_2\cos\phi - P_4\cos(k_1\phi) \\ \qquad\qquad +P_3\sin(k_1\phi)/k_1 + 1 \\ u_{cr2}\ (\phi) = P_1\sin\phi + P_2\cos\phi + P_4\cos(k_1\phi) \\ \qquad\qquad -P_3\sin(k_1\phi)/k_1 - M \end{cases} \tag{4}$$

where $\phi = 2\pi f_r t$, $f_r = 1/(2\pi\sqrt{L_{r1}C_{r1}}) = 1/(2\pi\sqrt{L_{r2}C_{r2}})$, $k_1 = \sqrt{1/(1+2k)}$, $k = L_m/L_{r1}$, and $M = U_{\text{out}}/U_{\text{in}}$. $P_1$, $P_2$, $P_3$, $P_4$, and $M$ are the undetermined coefficients.

According to (4), both the current of the resonant inductor ($i_p$ and $i_s$) and the voltage of the resonant capacitor ($u_{cr1}$ and $u_{cr2}$) consist of two different frequency components. One is at $f_r$, the other is at $k_1 f_r$.

Based on (4), the sums of $i_p$, $i_s$ and $u_{cr1}$, $u_{cr2}$ can be calculated as

$$\begin{cases} i_p(\phi) + i_s(\phi) = 2P_1\cos\phi - 2P_2\sin\phi \\ u_{cr1}(\phi) + u_{cr2}\ (\phi) = 2P_1\sin\phi + 2P_2\cos\phi - M + 1. \end{cases} \tag{5}$$

Furthermore, it can be derived that

$$[i_p + i_s]^2 + [u_{cr1} + u_{cr2} - (1-M)]^2 = 4\left(P_1^2 + P_2^2\right). \tag{6}$$

According to (5), both $i_p + i_s$ and $u_{cr1} + u_{cr2}$ only have one frequency component, which is $f_r$. From (6), it can be known that the trajectory of $(i_p + i_s,\ u_{cr1} + u_{cr2})$ is a circle, and the center of the circle is $[(U_{\text{in}} - U_{\text{out}})/u_{\text{base}}, 0]$ (i.e., $[1-M, 0]$).

If selecting $i_p + i_s$ and $u_{cr1} + u_{cr2}$ as state variables, the operating process of the P Mode is equivalent to a simple *LC* resonance. Its equivalent circuit is shown in Fig. 4(d), where $U_{\text{dc}} = U_{\text{in}} - U_{\text{out}}$, $L = L_{r1} = L_{r2}$, and $C = C_{r1} = C_{r2}$.

Similarly, if selecting $i_p + i_s$ and $u_{cr1} + u_{cr2}$ as state variables for the O and N Modes, their operating processes are also equivalent to a simple LC resonance. Their equivalent circuit can also be expressed by Fig. 4(d), but $U_{\text{dc}}$, $L$, and $C$ will be different. Additionally, the values of $U_{\text{dc}}$ in the positive half-cycle and the negative half-cycle are opposites. The values of $U_{\text{dc}}$, $L$, and $C$ for the P Mode, N Mode, and O Mode are listed in Table II.

In Table II, $u_{cr2,\max}$ means the maximum value of $u_{cr2}$, and it is equal to the value of $u_{cr2}$ during the O Mode because $i_s$ is zero during the O Mode. The value of $u_{cr2,\max}$ is calculated as

$$u_{cr2,\max} = \frac{1}{2C_{r2}}\int_{t_1}^{t_2} i_s dt \tag{7}$$

where $t_1$ and $t_2$ are defined in Fig. 3.

According to the analysis above-mentioned, the P, N, O Modes can be expressed by a unified equivalent circuit and their operating processes are equivalent to simple *LC* resonance. This is the proposed state trajectory model for the *CLLC* converter. With this model, the state trajectory method can also be used to simplify the analysis of the *CLLC* converter.

TABLE II
VALUE OF PARAMETERS IN FIG. 4(D) FOR P, N, AND O MODE

| | $U_{dc}$(the positive half cycle) | $U_{dc}$(the negative half cycle) | $L$ | $C$ |
|---|---|---|---|---|
| P Mode | $U_{in} - U_{out}$ | $-U_{in} + U_{out}$ | $L_{r1}$ *or* $L_{r2}$ | $C_{r1}$ *or* $C_{r2}$ |
| N Mode | $U_{in} + U_{out}$ | $-U_{in} - U_{out}$ | $L_{r1}$ *or* $L_{r2}$ | $C_{r1}$ *or* $C_{r2}$ |
| O Mode | $U_{in} + u_{cr2,max}$ | $-U_{in} - u_{cr2,max}$ | $L_{r1} + L_m$ | $C_{r1}$ |

TABLE III
PARAMETERS OF THE STUDY CASE FOR TOLERANCE ANALYSIS

| Resonant tank and load condition | | | |
|---|---|---|---|
| $L_{r1}$ | 35uH | $C_{r1}$ | 34nF |
| Variation of $L_{r2}$ | 31.5uH-38.5uH | Variation of $C_{r2}$ | 30.6nF-37.4nF |
| $L_m$ | 386uH | $R_L$ | 160Ω |
| Working points | | | |
| $f_s$ | 80kHz | 105kHz | 130kHz |

TABLE IV
INFLUENCE OF THE VARIATION OF $L_{r2}$ AND $C_{r2}$ ON STATE TRAJECTORY MODEL

| $f_s$ | 80kHz | 105kHz | 130kHz |
|---|---|---|---|
| Disturbance on state trajectory | 1.07%; -1.07% | 0.96%; -0.57% | 2.51%; -2.51% |

The influence of components tolerance on the state trajectory model is investigated using the Monte Carlo method. A $\pm 10\%$ variance of $L_{r2}$ and $C_{r2}$ to $L_{r1}$ and $C_{r1}$ is taken in the analysis. Detailed parameters of the study case are listed in Table III.

The parameters of resonant tank shown in Table III are the same with that of the experimental prototype. Three working points are chosen to perform the Monte Carlo analysis. In order to calculate enough evaluation results for Monte Carlo analysis, 500 independent random samples are taken for $L_{r2}$ and $C_{r2}$.

For every sample of $L_{r2}$ and $C_{r2}$, the actual state trajectory (defined as disturbed trajectory) together with the state trajectory when $L_{r1} = L_{r2}$ and $C_{r1} = C_{r2}$ (defined as original trajectory) are calculated. The trajectory disturbance is used to quantify the influence of components tolerance. The trajectory disturbance is defined as the difference of $u_{cr1} + u_{cr2}$ between the original trajectory and disturbed trajectories when $i_p + i_s$ is a fix value. The percentages occupied by maximum trajectory disturbance are calculated and listed in Table IV.

According to the above-mentioned analysis, a $\pm 10\%$ variation in $L_{r2}$ and $C_{r2}$ only cause a maximum $\pm 2.51\%$ disturbance on the state trajectory. The influence caused by the variation of $L_{r2}$ and $C_{r2}$ is not significant. As a result, the proposed

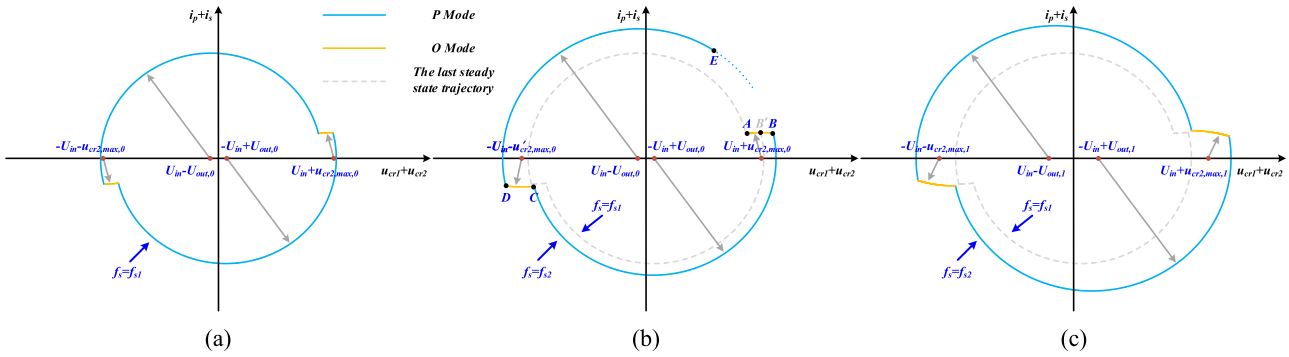


Fig. 5. (a) Steady-state trajectory at $f_{s1}$. (b) Transient trajectory when $f_s$ changes from $f_{s1}$ to $f_{s2}$. (c) Steady-state trajectory at $f_{s2}$.

state trajectory model is still valid considering the tolerance of inductors and capacitors of the resonant tank.

### C. State-Trajectory Analysis for the Load Transient in CLLC Converters

In the following section, we will use the proposed state-trajectory model to give a comprehensive analysis of the transient process in the resonant tank and clarify how $i_o$ is influenced by the control (i.e., the change of $f_s$) during the load transient.

There are two kinds of transient processes during the load transient. One is the charging and discharging process of $C_{\text{out}}$, which was analyzed in Section II-A. The other is the transient process in the resonant tank, which is caused by the change of $f_s$. The charging and discharging process of $C_{\text{out}}$ is usually at the millisecond (ms) level, while the transient process in the resonant tank is at the switching-period level. Generally, the switching frequency of the *CLLC* converter is hundreds of kHz, so the transient process in the resonant tank is at the microsecond ($\mu$s) level.

In the situation of a load increase, suppose $f_s = f_{s1} < f_r$ before load transient. Then, the converter will work in PO Mode [32]. The steady-state trajectory at $f_{s1}$ is illustrated in Fig. 5(a). Before the load increase, $U_{\text{out}} = U_{\text{out},0}$ , $u_{cr2,\max} = u_{cr2,\max,0}$ , and $i_c = 0$. Once the load increase is detected, the controller will decrease the switching frequency. The transient process in the resonant tank will start. If $f_s$ is changed from $f_{s1}$ to $f_{s2}$ ($f_{s2} < f_{s1}$), the transient trajectory as $f_s$ changes from $f_{s1}$ to $f_{s2}$ is illustrated in Fig. 5(b).

After a short time (several switching periods), the value of $U_{\text{out}}$ will only change slightly and can be seen as constant. The transient process in the resonant tank is as follows:

*Trajectory AB:* The trajectory AB is an O Mode trajectory. After $f_s$ is changed to $f_{s2}$, the transient process will start at the O Mode. Because $i_s = 0$ during the O Mode, $u_{cr2,\max}$ will not change and the center of the trajectory AB will still be ($U_{in} + u_{cr2,\max,0}$, 0). Since $f_{s2} < f_{s1}$, the time in O Mode increases. As a result, the trajectory AB will be longer than the trajectory AB'. The trajectory AB' is the O Mode trajectory at $f_{s1}$.

*Trajectory BC:* The trajectory BC is a P Mode trajectory. $U_{\text{out}}$ is not changed so the center of the trajectory will still be ($-U_{\text{in}} +$ $U_{\text{out}}$, 0). Because the trajectory AB is longer than the trajectory AB', the radius of the trajectory BC will be longer than that of the P Mode trajectory at $f_{s1}$ (i.e., the distance between the trajectory center and point B will be longer than the distance between the trajectory center and point B'). A longer radius of the P Mode trajectory means more energy is transferred from the primary side to the secondary side, so the value of $\text{mean}(i_{s,rec})$ will be larger. According to (1) and (7), $u_{cr2,\max}$ will be larger, too.

*Trajectory CD:* The trajectory CD is an O Mode trajectory. At point C, the value of $u_{cr2,\max}$ has increased to $u'_{cr2,\max,0}$. The trajectory center changes to ($-U_{\text{in}} - u'_{cr2,\max,0}$, 0), which is farther from (0, 0). The time of the O Mode will still be longer than that of the O Mode at $f_{s1}$, so the trajectory CD will also be longer than the trajectory AB'. All these factors make the radius of the next P Mode trajectory even longer.

*Trajectory DE:* The trajectory DE is a P Mode trajectory. The radius of the trajectory DE is longer, so even more energy is transferred, and $u_{cr2,\max}$ will be further increased at the end of the P Mode trajectory.

From the trajectory AB to DE, it can be known that if $f_s$ decreases, the radius of the P Mode trajectory will be longer after the O Mode, then more energy will be transferred to the secondary side during the P Mode. Such a process will repeat, and the state trajectory will expand. However, as more energy is transferred to the secondary side, $\text{mean}(i_{s,rec})$ will be larger than $i_o$. According to (2), $i_c > 0$, so $C_{\text{out}}$ will be charged and $U_{\text{out}}$ will increase. According to Table II, this process will make the radius of the next P Mode trajectory shorter. When the two processes achieve balance, the converter will enter the new steady state, as shown in Fig. 5(c). In the new steady state, $i_c$ is zero, $U_{\text{out}}$ increases to $U_{\text{out},1}$, and $i_o$ increases back to $i_{o,\text{set}}$. The load increase transient ends. The curve of $i_c$ during the load increase transient is illustrated in Fig. 7(a).

In practice, the controller will change $f_s$ continually before $i_o$ increases back to $i_{o,\text{set}}$ instead of just changing $f_s$ one time. As a result, the state trajectory of the converter will switch between the steady-state trajectory and the transient trajectory accordingly and finally end at the steady-state trajectory shown in Fig. 5(c).

In the situation of a load decrease, suppose $f_s = f_{s2}$ before the load transient. The steady-state trajectory at $f_{s2}$ is illustrated in Fig. 6(a). Before the load decrease, $U_{\text{out}} = U_{\text{out},0}$ ,

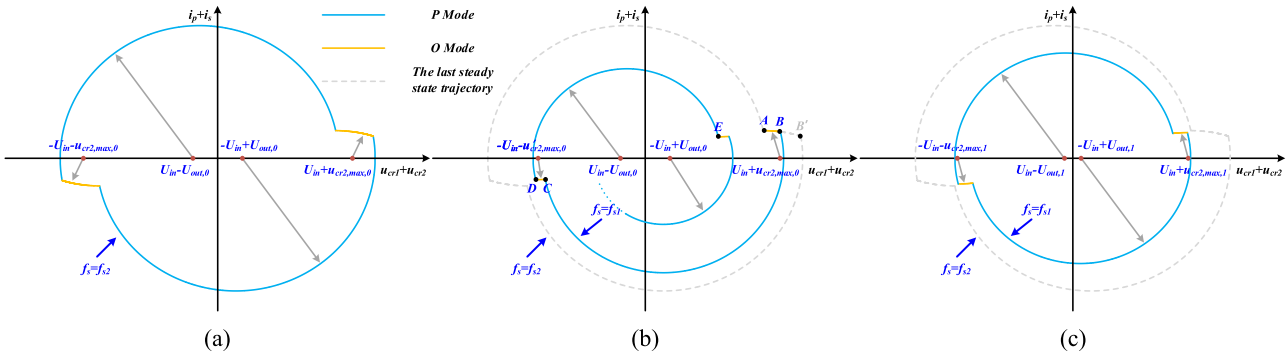


Fig. 6. (a) Steady-state trajectory at $f_{s2}$. (b) Transient trajectory when $f_s$ changes from $f_{s2}$ to $f_{s1}$. (c) Steady-state trajectory at $f_{s1}$.

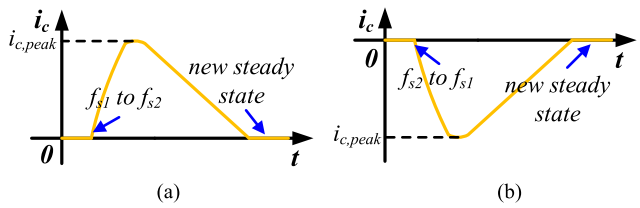


Fig. 7. Curves of $i_c$ after $f_s$ is changed. (a) Load increase. (b) Load decrease.

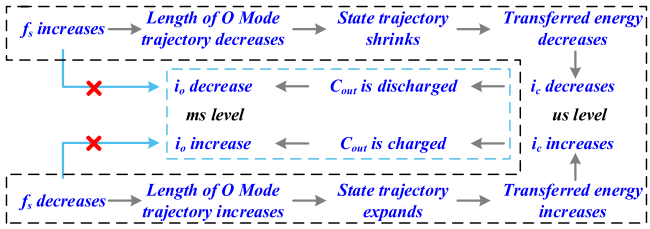


Fig. 8. Mechanism about how $f_s$ influences $i_o$.

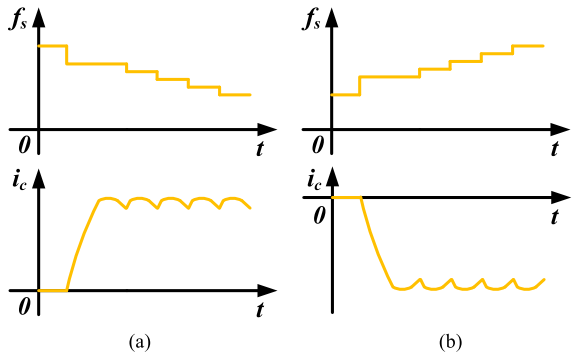


Fig. 9. Curves of $i_c$ after $f_s$ is changed continually. (a) Load increase. (b) Load decrease.

$u_{cr2,\max} = u_{cr2,\max,0}$ , and $i_c = 0$. Once the load decrease is detected, the controller will increase $f_s$. Suppose $f_s$ is changed from $f_{s2}$ to $f_{s1}$. The transient trajectory when $f_s$ changes from $f_{s2}$ to $f_{s1}$ is illustrated in Fig. 6(b). The radius of the P Mode trajectory will be shorter during the O Mode, and less energy will be transferred to the secondary side during the P Mode. Such a process repeats, and the state trajectory will shrink. As less energy is transferred to the secondary side, $C_{\text{out}}$ is discharged, and $U_{\text{out}}$ will decrease. This process will make the radius of the next P Mode trajectory longer. When the two processes achieve the balance, the converter will enter the new steady state, as shown in Fig. 6(c). In the new steady state, $i_c$ is zero, $U_{\text{out}}$ decreases to $U_{\text{out},1}$, and $i_o$ decreases back to $i_{o,\text{set}}$. The load decrease transient ends. The curve of $i_c$ during the load decrease transient is illustrated in Fig. 7(b). Similarly, the controller needs to change $f_s$ continually in practice. The state trajectory of the converter will also switch between the steady-state trajectory and the transient trajectory accordingly and finally end at the steady-state trajectory shown in Fig. 6(c).

Based on the state trajectory analysis, the mechanism of how $f_s$ influences $i_o$ is illustrated in Fig. 8. A change in $f_s$ does not cause $i_o$ to increase or decrease directly. Instead, the change in $f_s$ influences the transient process of the resonant tank directly, causing a change in $i_c$. The change in $i_c$ influences the charging and discharging process of $C_{\text{out}}$. As a result, $i_o$ will increase or decrease accordingly. The influence of $f_s$ on $i_c$ is at the $\mu$s level, but the influence of $i_c$ on $i_o$ is at the ms level. Generally, the control frequency is at the same time level as $f_s$, so during the time of a control period, the change in $f_s$ only has a weak and indirect influence on $i_o$, while the change in $f_s$ has a strong and direct influence on $i_c$.

### D. Relationship Between the Value of $i_c$ and the Change of $f_s$

According to Fig. 7, the relationship between $f_s$ and $i_c$ is not static but dynamic. The value of $i_c$ will eventually go back to zero after $f_s$ changes because $U_{\text{out}}$ will change. In order to keep $i_c > 0$ or $i_c < 0$ during the load transient, $f_s$ should change continually, as shown in Fig. 9.

In order to achieve good dynamic performance, the controller should change $f_s$ to make $|i_c|$ as large as possible during the load transient. This raises the question: what is the maximum (or minimal) value of $i_c$, and how it is achieved?

It has been known that the expanding (or shrinking) of the state trajectory will cause $i_c$ to increase (or decrease). So $i_c$ achieves its maximum (or minimal) value at the limit of the state trajectory expanding (or state trajectory shrinking).

The limit of the shrinking trajectory is zero. When the trajectory shrinks to zero, $\text{mean}(i_{s,rec})$ will be zero, too. According to (2), $i_c = -i_o$. This is the minimal value of $i_c$. If $f_s$ continues

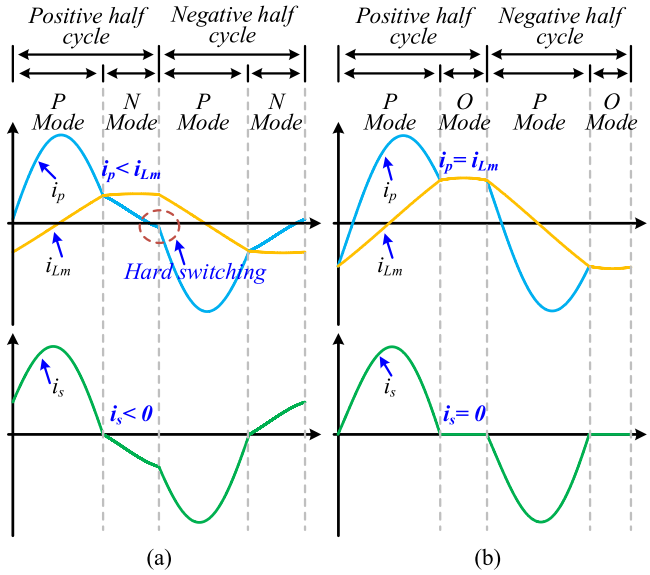


Fig. 10. Waveforms comparison of PN Mode and PO Mode. (a) PN Mode. (b) PO Mode.

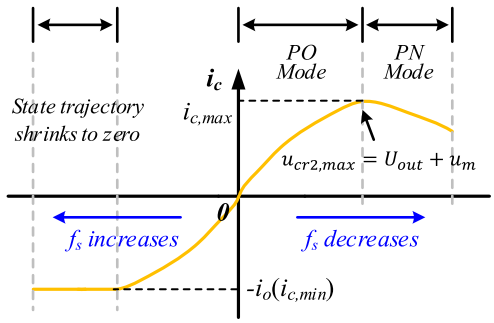


Fig. 11. Relationship between the change of $f_s$ and $i_c$.

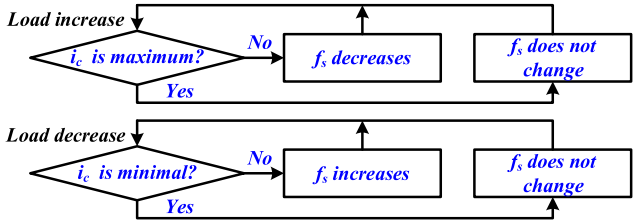


Fig. 12. Practical way to maintain $i_c$ at maximum (or minimal) value.

decreasing after the trajectory shrinks to zero, $i_c$ will not be changed by $f_s$.

The limit of the expanding trajectory is in the PN Mode. When the converter is shifting from the PO Mode to the PN Mode, $i_c$ reaches its maximum value. The waveforms comparison of the PN Mode and the PO Mode is illustrated in Fig. 10. The PN Mode should be avoided for the following reasons.

1) In the N Mode stage, $i_p < i_{Lm}$, so that $i_s < 0$. This decreases $\mathrm{mean}(i_{s,rec})$, according to (1), and makes $i_c$ smaller, according to (2).
2) In the N Mode stage, $i_p$ keeps decreasing, and the value of $i_p$ may be too small to fully charge the output capacitor of the primary side switches. The primary side switches may be under hard switching conditions, causing higher switching loss, voltage spike, and electromagnetic interference.

The criterion to judge whether the converter is working under the PN Mode or the PO Mode is as follows. If

$$u_{cr2,\max} > U_{\mathrm{out}} + u_m \tag{8}$$

is satisfied, the converter is working under the PN Mode. $u_m$ is the voltage across $L_m$. According to (1) and (7), it can be derived as

$$u_{cr2,\max} = \frac{T_s}{4C_{r2}} \mathrm{mean}\left(i_{s,rec}\right). \tag{9}$$

From (9), it can be known that as the state trajectory expands, $u_{cr2,\max}$ will increase. If $f_s$ keeps decreasing, the state trajectory will expand continually, and $u_{cr2,\max}$ will also increase continually. As a result, (8) will eventually be satisfied, and the converter will work under the PN Mode. If $f_s$ continues decreasing after the converter reaches the PN Mode, $i_c$ will decrease due to $f_s$.

The relationship between $f_s$ and $i_c$ is illustrated in Fig. 11. When $f_s$ is at a value that satisfies $u_{cr2,\max} = U_{\mathrm{out}} + u_m$, $i_c$ reaches its maximum value. When $f_s$ is at a value that makes the state trajectory shrink to zero, $i_c$ reaches its minimal value.

## III. Proposed Constant Current Control Method With Improved Dynamic Performance

### A. Way to Achieve the Maximum (or Minimal) $i_c$ and the Limitation of the Conventional PI Method

In Section II-D, two questions are raised: what is the maximum (minimal) value of $i_c$, and how it is achieved? The first question is answered in the above-mentioned analysis. In this section, the way to achieve the maximum (minimal) value of $i_c$ in the control is discusssed.

The *CLLC* converter is a highly nonlinear system. According to Fig. 11, $f_s$ should be set at a certain value to achieve the maximum (or minimal) $i_c$. However, this value of $f_s$ is difficult to calculate. To make matters worse, this value of $f_s$ changes with time. Since $i_c \neq 0$, $C_{\mathrm{out}}$ will be charged or discharged and $U_{\mathrm{out}}$ will change. As $U_{\mathrm{out}}$ changes, $u_{cr2,\max}$ may become less than $U_{\mathrm{out}} + u_m$, or the state trajectory may not be zero anymore. As a result, trying to calculate a certain value of $f_s$ online in the controller is not practical.

Alternatively, if the controller can judge whether $i_c$ is at its maximum (or minimal) value, $i_c$ can be maintained at its maximum (or minimal) value without calculating the value of $f_s$ (the diagram is illustrated in Fig. 12).

1) *During load increase:* Decrease $f_s$ if $i_c$ is not at its maximum value. Stop changing $f_s$ if $i_c$ is at its maximum value.
2) *During load decrease:* Increase $f_s$ if $i_c$ is not at its minimal value. Stop changing $f_s$ if $i_c$ is at its maximum value.

Based on the analysis abovementioned, the limitation of the conventional PI method is discussed. In the PI control method,

$i_o$ is the feedback variable, and $f_s$ is calculated as follows:

$$f_s = k_p\ (i_o - i_{o,\mathrm{set}}) + k_i \sum_{1}^{n} (i_o - i_{o,\mathrm{set}})\,\Delta t \qquad (10)$$

where $\Delta t$ is the control period. $k_p$ and $k_i$ are the PI controller parameters.

Since $f_s$ only has a weak and indirect influence on $i_o$ in the time of one control period, if $f_s$ is changed in one control cycle, $i_o$ will remain almost unchanged in the next control cycle. Using $i_o$ as a feedback variable will cause considerable delay in the control. This delay combined with the hysteresis of the integral term in the PI method will cause unavoidable overshoot in the response.

Moreover, the PI controller cannot realize good control of $i_c$ using (10). Using (10) to calculate $f_s$ will not maximize (or minimize) $i_c$, and (10) cannot tell if $i_c$ is at its maximum (minimal) value. For an increasing load, if $u_{cr2,\max} = U_{\mathrm{out}} + u_m$ is satisfied before $i_o$ reaches $i_{o,\mathrm{set}}$, $f_s$ will still decrease according to (10). Then $u_{cr2,\max}$ will be larger than $U_{\mathrm{out}} + u_m$ and the converter will enter the PN Mode. $i_c$ will decrease instead, and the primary side MOSFET may be under hard switching conditions. As a result, it will take more time for $i_o$ to go back to $i_{o,\mathrm{set}}$, and higher voltage spike and more electromagnetic interference will be caused. These are the limitations of the conventional PI method.

### *B. Feedback Variable of the Proposed Constant Current Control Method*

The key to implementing the idea shown in Fig. 12 is to determine if $i_c$ is at its maximum (or minimal) value, which cannot be realized by using $i_o$ as the feedback variable. According to (2), $i_c$ is determined by $\mathrm{mean}(i_{s,rec})$ and $i_o$. $i_o$ is associated with the charging and the discharging process of $C_{\mathrm{out}}$, which is at the $ms$ level, and $\mathrm{mean}(i_{s,rec})$ is associated with the transient process in the resonant tank, which is at the $us$ level. Thus, the change of $i_c$ is also at the $us$ level and is mainly determined by $\mathrm{mean}(i_{s,rec})$ rather than $i_o$.

According to the analysis in Section II-D, when the state trajectory shrinks to zero, $i_c$ is minimal and $\mathrm{mean}\ (i_{s,rec}) = 0$. According to (9), $u_{cr2,\max}$ is also zero at this moment. The value of $u_{cr2,\max}$ can be used to determine if $i_c$ is minimal.

When the converter is operating under the critical condition between the PO Mode and the PN Mode, $i_c$ is maximum. At this point, $u_{cr2,\max} = U_{\mathrm{out}} + u_m$. This criterion can be used to judge if $i_c$ is maximum. However, it is difficult to apply this criterion because the specific value of $u_m$ varies and is difficult to calculate online.

Fortunately, by applying the mode analysis method [32], the value of $u_{cr2,\max}/U_{\mathrm{out}}$ when the converter is at the critical point can be obtained by numerical calculation. The critical curves of $u_{cr2,\max}/U_{\mathrm{out}}$ vs. $f_s/f_r$ under different values of $k$ ($k = L_m/L_{r1}$ as defined in (3)) are illustrated in Fig. 13. $k$ is a constant parameter of the resonant tank. Then, critical curves of $u_{cr2,\max}/U_{\mathrm{out}}$ can be used to judge if $i_c$ is maximum.

From the above-mentioned analysis, $u_{cr2,\max}$ can be used to judge if $i_c$ is at its maximum (or minimal) value. As a result, $u_{cr2,\max}$ is used as the feedback variable in the proposed constant current method.

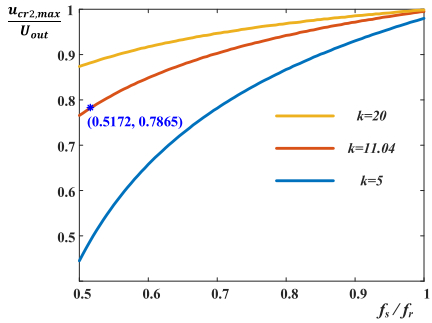


Fig. 13. Critical curves of $u_{cr2,\max}/U_{\mathrm{out}}$ versus $f_s/f_r$ under different $k$.

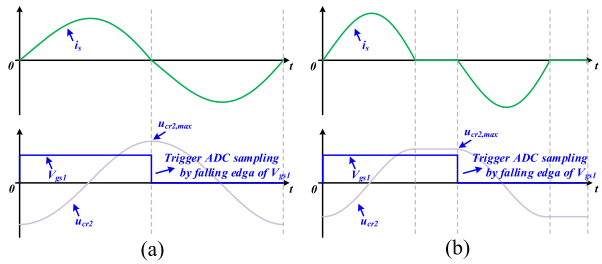


Fig. 14. Waveforms of $i_s$, $u_{cr2,\max}$, and $V_{gs1}$. (a) In the P Mode. (b) In the PO Mode.

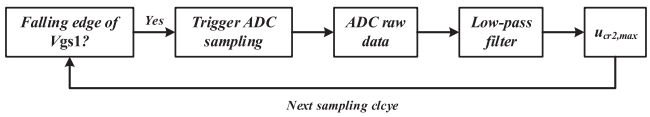


Fig. 15 Flowchart of the sampling scheme for $u_{cr2,\max}$.

The sampling of $u_{cr2,\max}$ is not difficult. As addressed in Section II, the proposed method targets at the case where the switching frequency is not larger than the resonant frequency (i.e., $f_s \le f_r$). As a result, the converter works under the P Mode ( $f_s = f_r$ ) or the PO Mode ($f_s < f_r$). Waveforms of $i_s$, $u_{cr2,\max}$, and $V_{gs1}$ in the P Mode and the PO Mode are illustrated Fig. 14(a) and (b). In Fig. 14, $V_{gs1}$ is the drive signal of $S_1$. According to Fig. 14, the value of $u_{cr2}$ always equals to $u_{cr2,\max}$ at moment of $V_{gs1}$'s falling edge. For the sampling of $u_{cr2,\max}$, it is not necessary to sample $u_{cr2}$ at a very high frequency to detect $u_{cr2,\max}$. Instead, controller just needs to trigger ADC sampling at the falling edge of $V_{gs1}$, and the value of $u_{cr2,\max}$ is automatically sampled. The flowchart of the sampling scheme for $u_{cr2,\max}$ is illustrated in Fig. 15.

### *C. Dead-Band-Based Method With Improved Dynamic Performance*

Since $u_{cr2,\max}$ can enable the controller to judge if $i_c$ is at its maximum (or minimal) value, the idea illustrated in Fig. 12 can be implemented in practice. Based on that, a novel dead-band-based control method with improved dynamic performance is proposed. The detailed step-by-step flow chart of the proposed dead-band-based method is illustrated in Fig. 16(a),

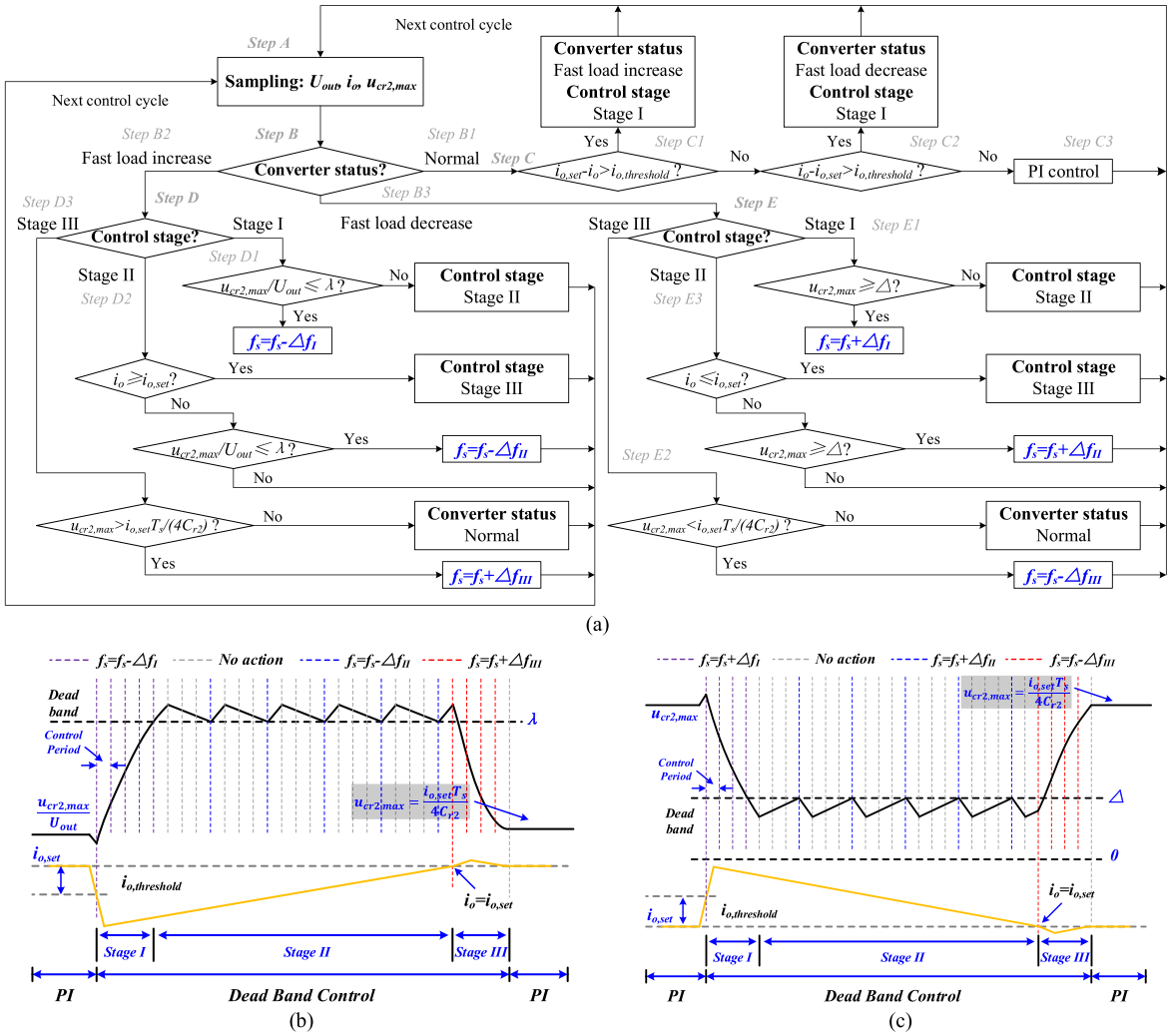


(a)




(b)




(c)

Fig. 16. (a) Step-by-step flow chart of the proposed dead-band-based method; Graphical diagrams of the proposed control method. (b) Under the load increase. (c) Under the load decrease.

and graphical diagrams of the proposed method under the load increase and the load decrease are illustrated in Fig. 16(b) and (c), respectively. The detailed implementation steps of the proposed method are as follows.

*Step A:* Update new sampling results for $U_{\rm out}$, $i_o$, and $u_{cr2,\max}$.

*Step B:* Judge the status of converter.

*Step B1:* If the converter is under normal status (normal status means the converter is under steady state or the load changes slowly), go to Step C.

*Step B2:* If the converter is under the status of fast load increase, go to Step D.

*Step B3:* If the converter is under the status of fast load decrease, go to Step E.

*Step C:* Detect the event of fast load transient.

*Step C1:* If $i_{o,\rm set}-i_o>i_{o,\rm threshold}$ is satisfied, set the converter status as fast load increase and set the control stage as Stage I. Then go back to Step A. Otherwise, go to Step C2.

*Step C2:* If $i_o-i_{o,\rm set}>i_{o,\rm threshold}$ is satisfied, set the converter status as fast load decrease and set the control stage as Stage I. Then go back to Step A. Otherwise, go to Step C3.

*Step C3:* The converter is still under normal status, a PI controller is used to regulate $i_o$. Then go back to Step A.

*Step D:* Handle fast load increase transient. If the type of control stage is Stage I, go to Step D1; If the type of control stage is Stage II, go to Step D2; If the type of control stage is Stage III, go to Step D3.

*Step D1:* If $u_{cr2,\max}/U_{\rm out}\leq\lambda$ is satisfied, $f_s$ is reduced by $\Delta f_I$ (i.e., $f_s=f_s-\Delta f_I$) and go back to Step A. Otherwise, set the control stage as Stage II and go back to Step A.

*Step D2:* If $i_o\geq i_{o,\rm set}$ is satisfied, set the control stage as Stage III and go back to Step A. Otherwise, if $u_{cr2,\max}/U_{\rm out}\leq\lambda$ is satisfied, $f_s$ is reduced by $\Delta f_{II}$ (i.e., $f_s=f_s-\Delta f_{II}$) and go back to Step A, if $u_{cr2,\max}/U_{\rm out}\leq\lambda$ is not satisfied, $f_s$ is not changed and go back to Step A.

*Step D3:* If $u_{cr2,\max}>i_{o,\rm set}T_s/(4C_{r2})$ is satisfied, $f_s$ is increased by $\Delta f_{III}$ (i.e., $f_s=f_s+\Delta f_{III}$) and go back to Step A. Otherwise, set the converter status as normal and go

back to Step A. The expression $i_{o,\text{set}}T_s/(4C_{r2})$ is new steady state value of $u_{cr2}$ according to (9).

*Step E:* Handle fast load decrease transient. If the type of control stage is Stage I, go to Step E1; If the type of control stage is Stage II, go to Step E2; If the type of control stage is Stage III, go to Step E3.

*Step E1:* If $u_{cr2,\max} \geq \Delta$ is satisfied, $f_s$ is increased by $\Delta f_I$ (i.e., $f_s = f_s + \Delta f_I$) and go back to Step A. Otherwise, set the control stage as Stage II and go back to Step A.

*Step E2:* If $i_o \leq i_{o,\text{set}}$ is satisfied, set the control stage as Stage III and go back to Step A. Otherwise, if $u_{cr2,\max} \geq \Delta$ is satisfied, $f_s$ is increase by $\Delta f_{II}$ (i.e., $f_s = f_s + \Delta f_{II}$) and go back to Step A, if $u_{cr2,\max} \geq \Delta$ is not satisfied, $f_s$ is not changed and go back to Step A.

*Step E3:* If $u_{cr2,\max} < i_{o,\text{set}}T_s/(4C_{r2})$ is satisfied, $f_s$ is decrease by $\Delta f_{III}$ (i.e., $f_s = f_s - \Delta f_{III}$) and go back to Step A. Otherwise, set the converter status as normal and go back to Step A.

In Fig. 16(a), $i_{o,\text{threshold}}$ is a threshold value used to detect the fast load transient event. λ and Δ are dead band boundaries for fast load increase and fast load decrease, respectively. $\Delta f_I$, $\Delta f_{II}$, and $\Delta f_{III}$ are adjustment for $f_s$ in control stage of Stage I, Stage II, and Stage III, respectively.

The value of $i_{o,\text{threshold}}$ is determined by users which depends on how large a load transient being seen as a fast load transient. The value of Δ should be small but larger than zero. According to Fig. 13, λ changes by $f_s$ if maintaining $i_c$ at the maximum value exactly. As a result, a lookup table needs to be established, and the controller checks the table every control cycle. To simplify the control method, a tradeoff is made. The value of λ is set as the value of $u_{cr2,\max}/U_{\text{out}}$ when $f_s$ is minimal. By maintaining $u_{cr2,\max}/U_{\text{out}}$ at λ, a large enough $i_c$ can be achieved and the converter also works under the PO Mode.

Other control parameters is determined as follows. The value of $\Delta f_I$ should be relatively large so that $u_{cr2,\max}/U_{\text{out}}$ or $u_{cr2,\max}$ reaches the bead-band boundary quickly. However, if $\Delta f_I$ is too big, the converter may operate under the PN mode during Stage I in a load increase. A suitable value for $\Delta f_I$ is 1 kHz – 5 kHz. $\Delta f_{II}$ should be smaller than $\Delta f_I$ because in Stage II, the controller only needs to maintain $u_{cr2,\max}/U_{\text{out}}$ or $u_{cr2,\max}$ at the dead-band boundary. Several hundred hertz is suitable. $\Delta f_{III}$ should be even smaller to make the converter enter the new steady state smoothly to prevent overshoot.

The proposed method is also suitable reverse operation. The input side and output side in forward operation and reverse operation are opposite. As a result, In reverse mode, $S_5$ to $S_8$ are inverter side, $S_1$ to $S_4$ are rectifier side, and $u_{cr1.\max}$ , $U_{in}$, and $i_{in}$ is used in control.

## IV. Experimental Verification

A prototype is built to verify the proposed dead-band-based constant current control method. The figure and the parameters of our experimental prototype are given in Fig. 17 and Table V, respectively.

The $k$ value of this prototype is $L_m/\ L_r = 386/35 = 11.04$. The minimal $f_s$ is set at 75 kHz. According to Fig. 13, the dead-band boundary λ is set as 0.78. Since the *CLLC* converter has a symmetric structure and the transformer turns ratio of experimental prototype is 1, waveforms of reverse operation are almost the same as that of forward operation. For the sake of simplicity, the forward operation is mainly focused on to demonstrate the effect of the proposed method.

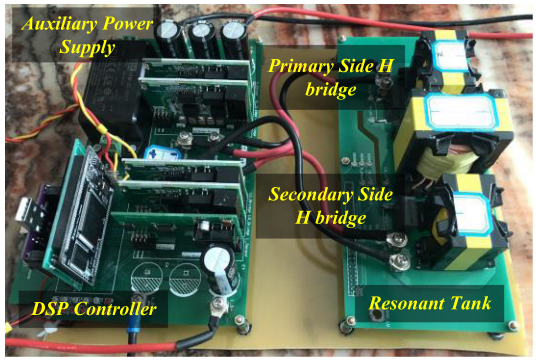


Fig. 17. Photograph of our experimental prototype.

TABLE V
Parameters of the Lab-Level Prototype

| | | | |
|---|---|---|---|
| General parameters | | | |
| DSP controller | TMS320F28335 | MOSFET | C3M0120090J |
| Output capacitance $C_{out}$ | | 100uF | |
| Input voltage | | 320V | |
| Target output current | | 2A | |
| Resonant Tank | | | |
| Turns ratio | 1 | $L_m$ | 386uH |
| $L_{r1}/L_{r2}$ | 35uH | $C_{r1}/C_{r2}$ | 34nF |
| Resonant frequency $f_r$ | | 145kHz | |
| Range of switching frequency | | 75kHz-145kHz | |
| Control Parameters | | | |
| $\lambda$ | 0.78 | $\Delta$ | 10V |
| $\Delta f_I$ | 2000Hz | $\Delta f_{II}$ | 500Hz |
| $\Delta f_{II}$ | 100Hz | $i_{o,threshold}$ | 6%*$i_{o,set}$ |

Fig. 18(a) shows the dynamic waveform of $U_{\text{out}}$ when $f_s$ changes from 110 to 100 kHz. The load resistance is 220 Ω There is a 340 V offset in the scope channel. After $f_s$ changed, $U_{\text{out}}$ increased gradually, which means $C_{\text{out}}$ was charged. In Fig. 18(b), waveforms of a smaller time scale are illustrated to show the transient process in the resonant tank. According to Fig. 18(b), the time of the O Mode increased after $f_s$ decreased to 100 kHz. The amplitudes of $i_p$, $i_s$, $u_{cr1}$, and $u_{cr2}$ also increased quickly, which meant more energy was transferred to the secondary side.

The experimental transient trajectory when $f_s$ changed from 110 to 100 kHz is illustrated in Fig. 18(f). The length of the O Mode trajectory increased and the whole trajectory expanded. Steady-state trajectories at 100 and 110 kHz are shown in Fig. 18(e). The steady-state trajectory at 100 kHz is larger. Similarly, when $f_s$ increased from 100 to 110 kHz, $U_{\text{out}}$ decreased gradually so that $C_{\text{out}}$ was discharged [see Fig. 18(c)]. In Fig. 18(d), the time of the O Mode decreased and the amplitudes of $i_p, i_s, u_{cr1}$, and $u_{cr2}$ also decreased quickly. Correspondingly, the length of the O Mode trajectory decreased and the whole trajectory shranks, as shown in Fig. 18(g). The experimental results

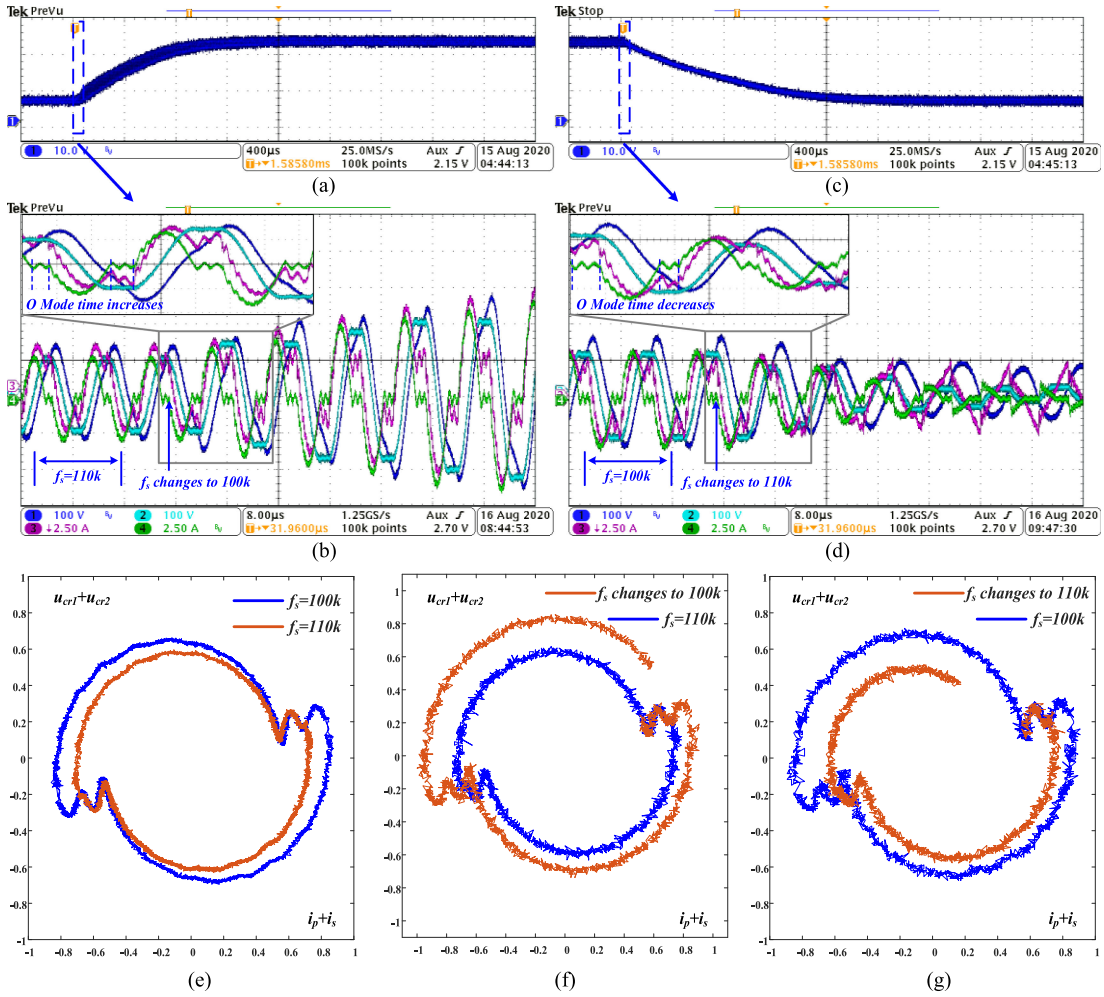


Fig. 18. Waveforms of $U_{\text{out}}$ when $f_s$ decreases (a) and increases (c). Dynamic processes in the resonant tank when $f_s$ decreases (b) and increases (d). CH1: $u_{cr1}$ CH2: $u_{cr2}$ CH3:$i_p$ CH4:$i_s$; (e) Experimental steady-state trajectory at 100 and 110 kHz. (f) Experimental transient trajectory when $f_s$ changes from 110 to 100 kHz. (g) Experimental transient trajectory when $f_s$ changes from 100 to 110 kHz.

of the transient process in the resonant tank are consistent with the state trajectory analysis in Section II-C. The correctness of the proposed state trajectory model and state trajectory analysis for the *CLLC* converter is verified.

The time span in Fig. 18(b) corresponds to the region marked by blue square in Fig. 18(a). Comparing Fig. 18(b) with Fig. 18(a), the amplitudes of $i_p$, $i_s$, $u_{cr1}$, and $u_{cr2}$ increased greatly, but $U_{\text{out}}$ only changed a little after $f_s$ decreased. Similarly, the time span in Fig. 18(d) corresponds to the region marked by the blue square in Fig. 18(c). The amplitudes of $i_p$, $i_s$, $u_{cr1}$, and $u_{cr2}$ decreased greatly while $U_{\text{out}}$ only changed a little after $f_s$ increased. Such differences prove that the transient process in the resonant tank is much faster than the charging and discharging process of $C_{\text{out}}$, as pointed out in Section II.

The dynamic performance comparisons between the proposed dead-band-based method and the conventional PI method in the load decrease and load increase conditions are illustrated in Fig. 19 and Fig. 20, respectively. The performance data are listed in Table VI. The target value of $i_o$ was set at 2 A (i.e., $i_{o,\text{set}} = 2$ A). In the experiment, the moment that $i_o$ first remains

TABLE VI
DYNAMIC PERFORMANCE COMPARISON BETWEEN THE PROPOSED DEAD-BAND-BASED METHOD AND THE CONVENTIONAL PI METHOD

| | | Proposed bead-band based method | Conventional PI method |
|---|---|---|---|
| Load increase condition | Response time | 5.3 ms (57.3% off) | 12.4 ms |
| | Overshoot | 0 | 0.16A (8%) |
| Load decrease condition | Response time | 5.6 ms (56.3% off) | 12.8 ms |
| | Overshoot | 0 | 0.16A (8%) |
| | Primary side MOSFET | ZVS | Hard switching |

in the range of (–3%+1, +3%+1) $i_{o,\text{set}}$ is regarded as the end of the transient process.

For a load increase, the load resistance changed from 160 to 220 Ω. According to Fig. 20(a) and (d), $i_o$ stepped down to 1.4 A (30% lower than $i_{o,\text{set}}$ and exceeding $i_{o,\text{threshold}}$) after the load increase. The conventional PI method took 12.8 ms to bring $i_o$ back to $i_{o,\text{set}}$, and a 0.16 A (8% of $i_{o,\text{set}}$) overshoot occurred. In contrast, the length of the transient process of the proposed

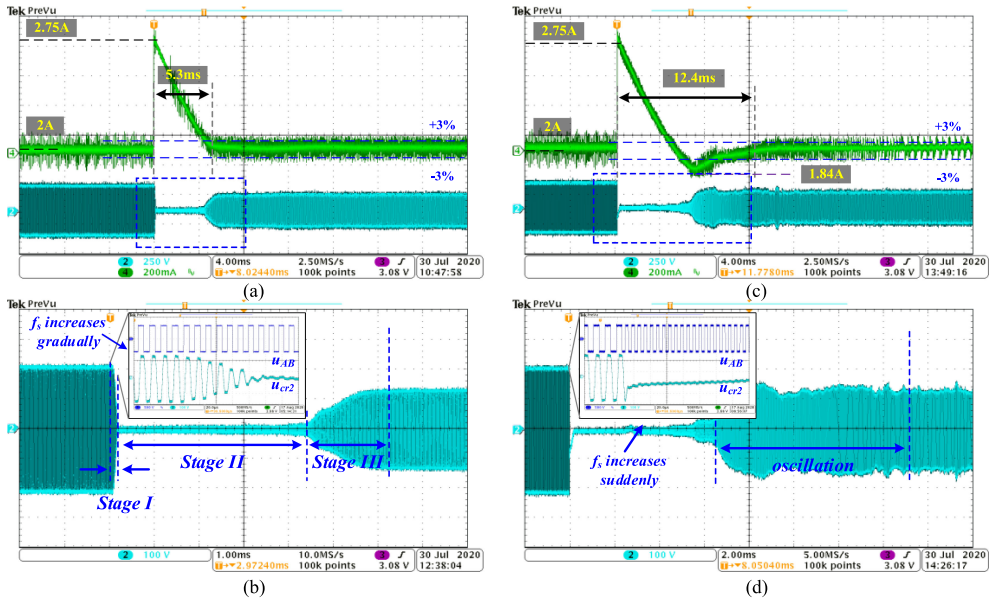


Fig. 19. Full response waveforms (a) and detailed $u_{cr2}$ and $u_{AB}$ waveforms (b) of the proposed dead-band-based method in load decrease condition; Full response waveforms (c) and detailed $u_{cr2}$ and $u_{AB}$ waveforms (d) of the conventional PI method in load increase condition; CH1: $u_{AB}$ CH2: $u_{cr2}$ CH4: $i_o$.

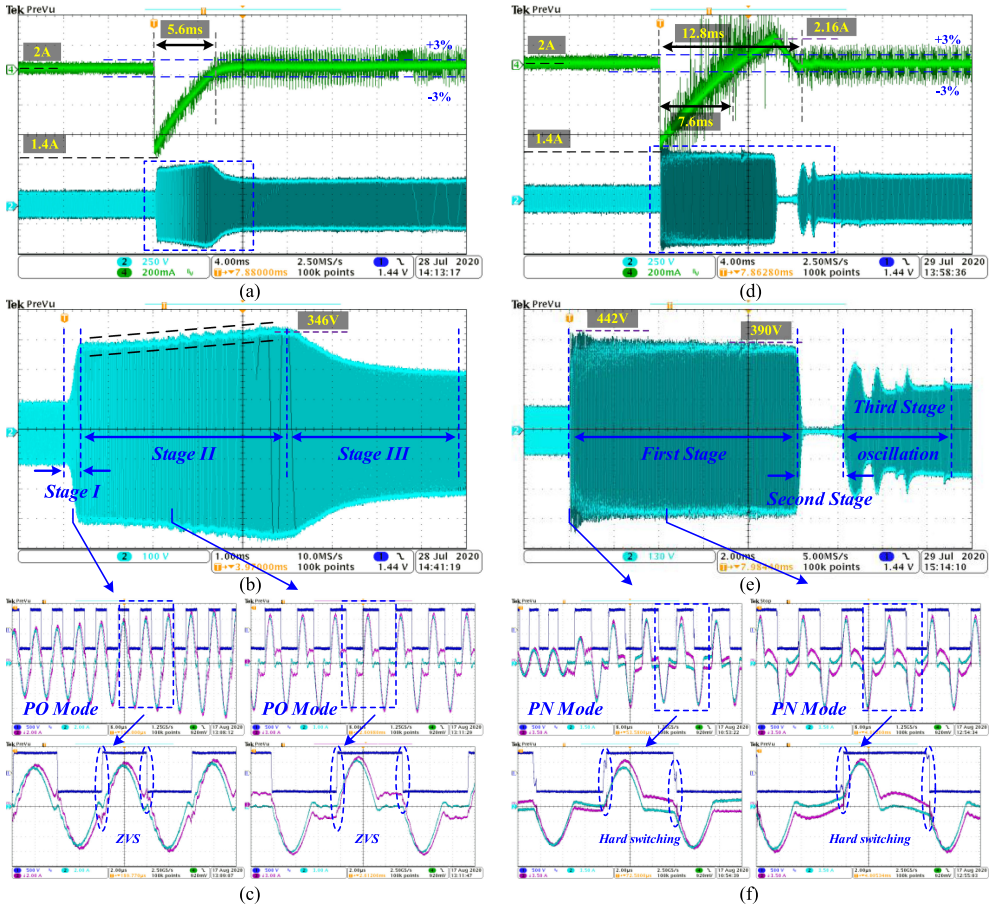


Fig. 20. Full response waveforms (a) and the detailed $u_{cr2}$ waveform (b) of the proposed dead-band-based method in the load increase condition; Full response waveforms (d) and the detailed $u_{cr2}$ waveforms (e) of the conventional PI method in the load increase condition; CH2: $u_{cr2}$ CH4: $i_o$. The transient process in the resonant tank of the proposed dead-band-based method (c) and the conventional PI method (f) during the load transient; CH1: $u_{AB}$ CH2: $i_p$ CH3: $i_s$.

dead-band-based method was only 5.6 ms, and no overshoot occurred.

According to Fig. 15, the proposed dead-band-based method during load increase also has three stages. The waveform of $u_{cr2}$ illustrated in Fig. 20 shows the three stages in practice. In *Stage I*, $u_{cr2,\max}$ increased quickly. The left figure in Fig. 20(c) shows the transient process in the resonant tank during *Stage I*. The amplitudes of $i_p$ and $i_s$ increased gradually as $f_s$ decreased gradually. In the waveform of $i_s$, the value of $i_s$ was maintained at zero after the P Mode. According to Fig. 10, the converter was working under the PO Mode. The value of $i_p$ was large enough to charge the output capacitor of the primary side MOSFET, and the ZVS condition was realized. In *Stage II*, $u_{cr2,\max}/U_{\text{out}}$ was maintained at $\lambda = 0.78$. In Fig. 20(b), $u_{cr2,\max}$ increased gradually during *Stage II*, it is because $C_{\text{out}}$ was charging and $U_{\text{out}}$ was increasing gradually. At the end of *Stage II*, $i_o$ reached $i_{o,\text{set}}$ so that $U_{\text{out}}$ was about 440 V, and $u_{cr2,\max}$ should be $U_{\text{out}} \times \lambda = 343.2$ V. The measured $u_{cr2,\max}$ at the end of *Stage II* is about 346 V, which means the proposed dead-band-based control method was operating correctly. The transient process in the resonant tank during *Stage II* is illustrated in the right figure of Fig. 20(f). The converter was also working under the PO Mode, and the ZVS condition was also achieved. In *Stage III*, after $i_o$ reached $i_{o,\text{set}}$, $u_{cr2,\max}$ decreased gradually to its new steady-state value.

For comparison, waveforms of $u_{cr2}$ and the transient process in the resonant tank of the conventional PI method are illustrated in Fig. 20(e) and (f). The waveform of $u_{cr2}$ can also be divided into three stages, as shown in Fig. 19(e).

In the first stage, $f_s$ was too small and $u_{cr2,\max}$ was too large (between 390 and 442 V). Formula (8) was satisfied and the converter was working under the PN Mode. The left figure in Fig. 20(f) shows the transient process in the resonant tank when the load resistance was changed. The value of $f_s$ decreased suddenly, while the amplitude of $i_p$ and $i_s$ increased very quickly. The value of $i_s$ was less than zero after the P Mode, so the converter was working under the PN mode according to Fig. 10. The value of $i_p$ at the MOSFET switching transient was too small to charge the output capacitor. As a result, the primary side MOSFET was under hard switching conditions. The right figure in Fig. 19(f) shows the transient process in the resonant tank at about the middle of the first stage. The converter was also working under the PN mode and the primary side MOSFET was under hard switching conditions.

Moreover, the waveform of $i_o$ under the PI method has many spikes compared to that of the proposed method. This is because the primary side MOSFET was under hard switching conditions, so the current probe was interfered. Working under PN mode also caused $C_{\text{out}}$ to be charged slower than that in our proposed method. In our method, it took 5.4 ms for $i_o$ to get back to the range of (–3%+1, +3%+1) $i_{o,\text{set}}$. However, in the PI method, it took 7.4 ms. Similar to the response during load decrease, the PI method failed to decrease $u_{cr2,\max}$ to its new steady-state value in time and caused overshoot. After the overshoot, in the second stage, the PI controller decreased $f_s$ to bring $i_o$ back. In the third stage, there was some oscillation before the converter finally entered the new steady state.

The experimental comparison shows that the dynamic response time of the proposed dead-band-based method during load transient is much shorter than that of the conventional PI method. No overshoot occurs and the ZVS condition is guaranteed during the transient process. The improved dynamic performance of the proposed dead-band-based constant current control method is verified.

## V. Conclusion

The charging and discharging process of the output capacitor determines the dynamic performance in constant current control. In this article, the state trajectory model is established for the *CLLC* converter and a comprehensive state trajectory analysis of the load transient process is performed under the constant current control. Using the state trajectory analysis, the mechanism about how $f_s$ influences $i_o$ is clarified. Based on our analysis, a novel constant current control method with improved dynamic performance over the conventional PI method is proposed for the *CLLC* converter. Our proposed method achieves direct and effective control of the charging and the discharging process of the output capacitor, which the conventional PI control method cannot achieve. As a result, dynamic performance is improved.

The correctness of the proposed state trajectory model, the state trajectory, and the effectiveness of the proposed dead-band-based constant current control method are verified by experiments. Experimental results show that, during the load increase transient, the ZVS condition is lost under the conventional PI method but is still guaranteed under the proposed method. Moreover, the response time of the proposed method is shortened by more than 50% compared to that of the conventional PI method, with no overshoot occurring.

## References


[1] W. Chen, P. Rong, and Z. Lu, "Snubberless bidirectional DC–DC converter with new *CLLC* resonant tank featuring minimized switching loss," *IEEE Trans. Ind. Electron.*, vol. 57, no. 9, pp. 3075–3086, Sep. 2010.

[2] J. Jung, H. Kim, M. Ryu, and J. Baek, "Design methodology of bidirectional *CLLC* resonant converter for high-frequency isolation of DC distribution systems," *IEEE Trans. Power Electron.*, vol. 28, no. 4, pp. 1741–1755, Apr. 2013.

[3] Z. U. Zahid, Z. M. Dalala, R. Chen, B. Chen, and J. Lai, "Design of bidirectional DC–DC resonant converter for vehicle-to-grid (V2G) applications," *IEEE Trans. Transp. Electrific.*, vol. 1, no. 3, pp. 232–244, Oct. 2015.

[4] X. Lu and H. Wang, "Three-port bidirectional *CLLC* resonant converter based onboard charger for PEV hybrid energy management system," in *Proc. IEEE Energy Convers. Congr. Expo.*, Cincinnati, OH, USA, 2017, pp. 1432–1438.

[5] P. He, A. Mallik, A. Sankar, and A. Khaligh, "Design of a 1-MHz high-efficiency high-power-density bidirectional GaN-based CLLC converter for electric vehicles," *IEEE Trans. Veh. Technol.*, vol. 68, no. 1, pp. 213–223, Jan. 2019.

[6] B. Liu, M. Qiu, L. Jing, X. Wang, and M. Chen, "Design of high-performance bidirectional DC/DC converter applied for more electric aircraft," *J. Eng.*, vol. 2018, no. 13, pp. 520–523, 2018.

[7] J. Huang, J. Xiao, C. Wen, P. Wang, and A. Zhang, "Implementation of bidirectional resonant DC transformer in hybrid AC/DC micro-grid," *IEEE Trans. Smart Grid*, vol. 10, no. 2, pp. 1532–1542, Mar. 2019.

[8] X. Lin, K. Sun, J. Lin, Z. Zhang, and W. Kong, "A multi-port bidirectional power conversion system for reversible solid oxide fuel cell applications," in *Proc. Int. Power Electron. Conf.*, Niigata, Japan, 2018, pp. 3460–3465.

[9] J. Min and M. Ordonez, "Bidirectional resonant CLLC charger for wide battery voltage range: Asymmetric parameters methodology," *IEEE Trans. Power Electron.*, vol. 36, no. 6, pp. 6662–6673, Jun. 2021.
[10] B. Zhao, X. Zhang, and J. Huang, "AI algorithm-based two-stage optimal design methodology of high-efficiency CLLC resonant converters for the hybrid AC–DC microgrid applications," *IEEE Trans. Ind. Electron.*, vol. 66, no. 12, pp. 9756–9767, Dec. 2019.
[11] S. Zou, J. Lu, A. Mallik, and A. Khaligh, "Modeling and optimization of an integrated transformer for electric vehicle on-board charger applications," *IEEE Trans. Transp. Electrific.*, vol. 4, no. 2, pp. 355–363, Jun. 2018.
[12] B. Li, Q. Li, and F. C. Lee, "High-frequency PCB winding transformer with integrated inductors for a bi-directional resonant converter," *IEEE Trans. Power Electron.*, vol. 34, no. 7, pp. 6123–6135, Jul. 2019.
[13] S. Zhao, Q. Li, F. C. Lee, and B. Li, "High-frequency transformer design for modular power conversion from medium-voltage AC to 400 VDC," *IEEE Trans. Power Electron.*, vol. 33, no. 9, pp. 7545–7557, Sep. 2018.
[14] B. Li, Q. Li, F. C. Lee, and Y. Yang, "A symmetrical resonant converter and PCB transformer structure for common mode noise reduction," in *Proc. IEEE Energy Convers. Congr. Expo.*, Cincinnati, OH, USA, 2017, pp. 5362–5368.
[15] B. Li, Q. Li, and F. C. Lee, "A WBG based three phase 12.5 kW 500 kHz CLLC resonant converter with integrated PCB winding transformer," in *Proc. IEEE Appl. Power Electron. Conf. Expo.*, San Antonio, TX, USA, 2018, pp. 469–475.
[16] Y. Xuan, X. Yang, W. Chen, T. Liu, and X. Hao, "A novel three-level CLLC resonant DC-DC converter for bidirectional EV charger in DC microgrids," *IEEE Trans. Ind. Electron.*, vol. 68, no. 3, pp. 2334–2344, Mar. 2021.
[17] C. Zhang, P. Li, Z. Kan, X. Chai, and X. Guo, "Integrated half-bridge CLLC bidirectional converter for energy storage systems," *IEEE Trans. Ind. Electron.*, vol. 65, no. 5, pp. 3879–3889, May 2018.
[18] W. L. Malan, D. M. Vilathgamuwa, and G. R. Walker, "Modeling and control of a resonant dual active bridge with a tuned CLLC network," *IEEE Trans. Power Electron.*, vol. 31, no. 10, pp. 7297–7310, Oct. 2016.
[19] B. Li, L. Jing, X. Wang, N. Chen, B. Liu, and M. Chen, "A smooth mode-switching strategy for bidirectional OBC base on V2G technology," in *Proc. IEEE Appl. Power Electron. Conf. Expo.*, Anaheim, CA, USA, 2019, pp. 3320–3324.
[20] T. Mishima and Y. Koga, "Variable frequency phase-difference controlled CLLC resonant bidirectional DC-DC converter featuring wide-range ZVS performance and reactive power reduction," in *Proc. IEEE Energy Convers. Congr. Expo.*, Portland, OR, USA, 2018, pp. 6283–6290.
[21] S. Zou, A. Mallik, J. Lu, and A. Khaligh, "Sliding mode control scheme for a CLLC resonant converter," *IEEE Trans. Power Electron.*, vol. 34, no. 12, pp. 12274–12284, Dec. 2019.
[22] H. Chen, K. Sun, H. Chong, Z. Zhang, Y. Zhou, and S. Mu, "A hybrid compensation scheme for the gate drive delay in CLLC converters," *IEEE J. Emerg. Sel. Topics Power Electron.*, vol. 9, no. 1, pp. 1119–1132, Feb. 2021.
[23] S. Zou, J. Lu, A. Mallik, and A. Khaligh, "Bi-directional CLLC converter with synchronous rectification for plug-in electric vehicles," *IEEE Trans. Ind. Appl.*, vol. 54, no. 2, pp. 998–1005, Mar./Apr. 2018.
[24] A. Sankar, A. Mallik, and A. Khaligh, "Extended harmonics based phase tracking for synchronous rectification in CLLC converters," *IEEE Trans. Ind. Electron.*, vol. 66, no. 8, pp. 6592–6603, Aug. 2019.
[25] Y. Wang, Y. Li, L. Jiang, and Y. Huang, "Yijia cao. PSO-based optimization for constant-current charging pattern for Li-ion battery," *Chin. J. Elect. Eng.*, vol. 5, no. 2, pp. 72–78, 2019.
[26] Y. Qin *et al.*, "A rapid lithium-ion battery heating method based on bidirectional pulsed current: Heating effect and impact on battery life," *Appl. Energy*, vol. 280, 2020, Art. no. 115957.
[27] B. Yang, "Topology investigation of front end DC/DC converter for distributed power system," Ph.D. dissertation, Bradley Dept. Elect. Comput. Eng., Virginia Polytech. Inst. State Univ., Blacksburg, VA, USA, 2003.
[28] H. Wu, S. Ji, F. C. Lee, and X. Wu, "Multi-channel constant current (MC3) LLC resonant LED driver," in *Proc. IEEE Energy Convers. Congr. Expo.*, Phoenix, AZ, USA, 2011, pp. 2568–2575.
[29] S. Huang, C. Lin, and T. Hung, "Analysis and implementation of LLC inverters for ozone-driven system with constant-current control," in *Proc. IEEE Int. Symp. Circuits Syst.*, Melbourne, VIC, USA, 2014, pp. 2433–2436.
[30] L. Zhang, B. Gu, J. Dominic, B. Chen, C. Zheng, and J. Lai, "A dead-time compensation method for parabolic current control with improved current tracking and enhanced stability range," *IEEE Trans. Power Electron.*, vol. 30, no. 7, pp. 3892–3902, Jul. 2015.
[31] R. G. Retegui, M. Benedetti, M. Funes, P. Antoszczuk, and D. Carrica, "Current control for high-dynamic high-power multiphase buck converters," *IEEE Trans. Power Electron.*, vol. 27, no. 2, pp. 614–618, Feb. 2012, doi: 10.1109/TPEL.2011.2158658.
[32] Z. Lv, X. Yan, Y. Fang, and L. Sun, "Mode analysis and optimum design of bidirectional CLLC resonant converter for high-frequency isolation of DC distribution systems," in *Proc. IEEE Energy Convers. Congr. Expo.*, Montreal, QC, Canada, 2015, pp. 1513–1520.
[33] R. Oruganti, J. J. Yang, and F. C. Lee, "Implementation of optimal trajectory control of series resonant converter," *IEEE Trans. Power Electron.*, vol. 3, no. 3, pp. 318–327, Jul. 1988.
[34] W. Feng, F. C. Lee, and P. Mattavelli, "Simplified optimal trajectory control (SOTC) for LLC resonant converters," *IEEE Trans. Power Electron.*, vol. 28, no. 5, pp. 2415–2426, May 2013.
[35] C. Fei, F. C. Lee, and Q. Li, "Soft start-up for high frequency LLC resonant converter with optimal trajectory control," in *Proc. IEEE Appl. Power Electron. Conf. Expo.*, Charlotte, NC, USA, 2015, pp. 609–615.
[36] C. Fei, Q. Li, and F. C. Lee, "Digital implementation of light-load efficiency improvement for high-frequency LLC converters with simplified optimal trajectory control," *IEEE J. Emerg. Sel. Topics Power Electron.*, vol. 6, no. 4, pp. 1850–1859, Dec. 2018.
[37] A. Nabih, M. Ahmed, Q. Li, and F. C. Lee, "Transient control and soft Start-up for 1 MHz LLC converter with wide input voltage range using simplified optimal trajectory control," *IEEE J. Emerg. Sel. Topics Power Electron.*, vol. 9, no. 1, pp. 24–37, Feb. 2021.
[38] J. Zeng, G. Zhang, S. S. Yu, and B. Zhang, "LLC resonant converter topologies and industrial applications—A review," *Chin. J. Elect. Eng.*, vol. 6, no. 3, pp. 73–84, 2020.

**Huan Chen** (Student Member, IEEE) received the B.E. degree in electrical engineering in 2018 from Tsinghua University, Beijing, China, where he is currently working toward the Ph.D. degree in electrical engineering.

His research interests include the isolated bidirectional dc–dc converter.

**Kai Sun** (Senior Member, IEEE) received the B.E., M.E., and Ph.D. degrees in electrical engineering from Tsinghua University, Beijing, China, in 2000, 2002, and 2006, respectively.

In 2006, he was with the Faculty of Electrical Engineering, Tsinghua University, where he is currently a Tenured Associate Professor (Research Professor). From September 2009 to August 2010, he was a Visiting Scholar with the Department of Energy Technology, Aalborg University, Aalborg, Denmark. From January to August 2017, he was a Visiting Professor with the Department of Electrical and Computer Engineering, University of Alberta, Edmonton, Canada. His research interests include power electronics for renewable generation systems, microgrids, and energy internet.

Dr. Sun is an Associate Editor for the IEEE TRANSACTIONS ON POWER ELECTRONICS, *IEEE Journal of Emerging and Selected Topics in Power Electronics*, *Journal of Power Electronics*, and *Chinese Journal of Electrical Engineering*. He was the TPC Vice Chair of IEEE Energy Conversion Congress and Exposition (ECCE2017) and IEEE ECCE-Asia2017, the Organization Committee Chair of IEEE eGrid2019, the Publicity Chair of IEEE ECCE2020, and the Technical Program Chair of IEEE eGrid2021. He also served as the General Co-Chair of 2018 International Future Energy Challenge (2018). He is PELS Asia Pacific Regional Vice Chair, PELS Beijing Chapter Chair, and PELS Electronic Power Grid Systems Technical Committee (TC8) Secretary. He was a recipient of Delta Young Scholar Award in 2013, and Youth Award of China Power Supply Society in 2017, and IEEE TRANSACTIONS ON POWER ELECTRONICS' Outstanding Reviewers Award in 2019. He is selected as IEEE PELS Distinguished Lecturer in 2021–2022.

**Languang Lu** received the B.S. degree from Jimei University, Xiamen, China, in 1990, the M.S. degree from Wuhan Transportation University, Wuhan, China, in 1993, and the Ph.D. degree from the Wuhan University of Technology, Wuhan, China, in 2001. He is an Associate Professor and a core member of Academician Ouyang Minggao's team with the School of Vehicles and Mobility, Tsinghua University, Beijing, China. He has more than 100 academic papers, 1 book, and 83 patents. His research interests include the integration, optimization, and control of automotive new powertrains system and battery management system.

Prof. Lu was the recipient of 5 Technology Awards. The latest achievement "performance optimization control and system integration design and application of Lithium-ion power battery for vehicle" won 2016 China automobile industry technology invention first prize.

**Shuoqi Wang** received the B.S. degree in 2017 from Tsinghua University, Beijing, China, where he is currently working toward the Ph.D. degree.

His research interests include dc microgrid optimal control and energy storage system management.

**Minggao Ouyang** received the B.E. degree from Central South University, Changsha, China, in 1982, the M.S. degree from Dalian Jiaotong University, Dalian, China, in 1984, and the Ph.D. degree from the Technical University of Denmark, Lyngby, Denmark, in 1993, all in energy engineering.

He is Changjiang Distinguished Professor and the leader of Advanced Powertrain System team with Tsinghua University, Beijing, China, where he is responsible for directing the research and development of Lithium-ion battery safety design and management, PEM fuel cell powertrain and hydrogen systems, engine control and hybrid powertrains, energy storage, and smart energy systems. Since 2007, he has been the Chief Scientist of the China National Key R&D Program of <New Energy Vehicles>.

Dr. Ouyang was a recipient of many national and international awards. He is the member of the Chinese Academy of Sciences and Editor-in-Chief for the international journal of eTransportation.